Nanoscale Advances

ROYAL SOCIETY OF CHEMISTRY

PAPER

Check for updates

Cite this: *Nanoscale Adv.*, 2022, **4**, 4871

On-surface synthesis of hydroxy-functionalized graphene nanoribbons through deprotection of methylenedioxy groups†

Manabu Ohtomo, *[a] Hironobu Hayashi, [b] Akitoshi Shiotari, ‡[c] Mayu Kawamura,[b] Ryunosuke Hayashi,[b] Hideyuki Jippo,[a] Junichi Yamaguchi,[a] Mari Ohfuchi,[a] Naoki Aratani, [b] Yoshiaki Sugimoto,[c] Hiroko Yamada [b] and Shintaro Sato*[a]

We demonstrate on-surface deprotection of methylenedioxy groups which yielded graphene nanoribbons (GNRs) with edges functionalized by hydroxy groups. While anthracene trimer precursors functionalized with hydroxy groups did not yield GNRs, it was found that hydroxy groups are first protected as methylenedioxy groups and then deprotected during the cyclo-dehydrogenation process to form GNRs with hydroxy groups. The X-ray photoemission spectroscopy and non-contact atomic force microscopy studies revealed that ~20% of the methylenedioxy turned into hydroxy groups, while the others were hydrogen-terminated. The first-principles density functional theory (DFT) study on the cyclo-dehydrogenation process was performed to investigate the deprotection mechanism, which indicates that hydrogen atoms emerging during the cyclo-dehydrogenation process trigger the deprotection of methylenedioxy groups. The scanning tunneling spectroscopy study and DFT revealed a significant charge transfer from hydroxy to the Au substrate, causing an interface dipole and the HOMO being closer to the Fermi level when compared with hydrogen-terminated GNR/Au(111). This result demonstrates on-surface deprotection and indicates a possible new route to obtain GNRs with desired edge functionalization, which can be a critical component for high-performance devices.

Received 14th January 2022
Accepted 4th October 2022

DOI: 10.1039/d2na00031h

rsc.li/nanoscale-advances

Introduction

The application of nanocarbon materials for electronic devices has progressed rapidly in the last few years. Graphene, for example, opens up new applications in optoelectronics,[1] such as infra-red and THz detectors[2] or optical switching devices.[3] The promising achievement of carbon nanotubes (CNTs), on the other hand, is a thermal-interface material (TIM) made from aligned CNTs,[4] field-effect transistors (FETs) with a small footprint,[5] and a RISC-V (reduced instruction set computer) processor with novel architecture in which degradation derived from metallic CNTs is taken care of.[6] Amid the rapid evolution of nanocarbon materials, atomically precise graphene nanoribbons (GNRs) were reported,[7] which enable us to overcome CNT's shortcomings of structural control and graphene's zero band gap.

While various bottom-up GNRs have been reported to date, including armchair GNRs with various widths,[8–10] zigzag GNRs,[11] OBO-edge GNRs,[12] and heterojunction GNRs with topologically nontrivial gap states,[13,14] theoretical predictions of device performances of extremely narrow GNRs have also been performed intensively, including the possibility of GNR tunneling field-effect transistors (TFETs)[15] and GNR backward diodes (BWDs).[16] The advantage of sub-nm wide GNRs fabricated by the bottom-up process is negligible junction capacitance. The GNR BWDs with a GNR heterojunction in the channel, in which one side of the GNR's edges is terminated by hydrogen while the other side is terminated by fluorine, can outperform state-of-the-art diodes made from compound semiconductors.[16] While the simulated performance is promising, there are a couple of significant challenges in the

[a]*Fujitsu Research, Fujitsu Limited, 10-1 Morinosato-Wakamiya, Atsugi, Kanagawa, 243-0197, Japan. E-mail: ohtomo.manabu@fujitsu.com; sato.shintaro@fujitsu.com*

[b]*Division of Materials Science, Nara Institute of Science and Technology, 8916-5 Takayama-cho, Ikoma, Nara 630-0192, Japan*

[c]*Department of Advanced Materials Science, The University of Tokyo, 5-1-5 Kashiwanoha, Kashiwa, Chiba 277-8561, Japan*

† Electronic supplementary information (ESI) available: Materials and methods for precursor synthesis, NMR and mass spectra of precursors, X-ray single-crystal analysis of precursors, comments on the stability of THO-DBTA, the models used for the first-principles evaluation of XPS binding energies, simulated nc-AFM images, analysis on the inter-GNR distance, the effect of hydroxy group distribution on the electronic properties of GNRs, the effect of edge functionalization on the hydrogen hopping paths, the band gap of free-standing GNRs, other possible paths for cyclo-dehydrogenation and the HOMO and LUMO of functionalized GNRs. See DOI: https://doi.org/10.1039/d2na00031h

‡ Present address: Department of Physical Chemistry, Fritz-Haber Institute of the Max-Planck Society, Faradayweg 4-6, 14195 Berlin, Germany.

This article is licensed under a Creative Commons Attribution-NonCommercial 3.0 Unported Licence.

(cc) BY-NC

experimental study of GNR devices.[17–22] A widely recognized challenge is fabricating sufficiently long GNRs with a moderate band gap. The bottom-up GNRs longer than ~100 nm reported so far[23,24] have a band gap larger than 1 eV and often suffer from contact problems.[17] Another challenge lies in fabricating well-defined heterojunctions of GNRs in the channel, which is mandatory for GNR TFETs or GNR BWDs.

There are several promising methods for fabricating GNR heterojunctions. The nanoscale heterojunctions were reported previously,[25,26] which were fabricated by subsequent deposition of precursors or post-annealing. The functionalization of GNR edges by electron-donating and electron-withdrawing groups can modify the highest-occupied molecular orbitals (HOMOs) and the lowest-unoccupied molecular orbitals (LUMOs) of GNRs. However, the bottom-up synthesis of edge-functionalized GNRs is challenging due to edge hydrogenation during cyclo-dehydrogenation.[27] During the cyclo-dehydrogenation process of anthracene polymers, hydrogen atoms are detached from the polymers after hopping to the edges. The hydrogenation of the edge carbon atoms can cleave edge functional groups, leaving hydrogen-terminated GNRs.[27] Consequently, a limited number of reports have been made on edge-functionalized GNRs so far,[28–30] while some failures have been reported as well.[31]

In this research study, we report on the bottom-up growth of GNRs with edges functionalized by hydroxy functional groups. To realize the synthesis of edge-hydroxylated GNRs, catechol units in the GNR precursor were protected by methylene acetal.[32] It is well known in organic chemistry that the resulting methylenedioxy protecting groups are relatively stable and efficiently deprotected by treatment with a suitable Lewis acid such as boron or aluminum halide.[32–34] However, more bulky acetal protection with alkyl chains is often preferred in solution synthesis from the viewpoints of solubility and easy detachment, while a bulky substituent could be an obstacle to the on-surface synthesis. Our study revealed that the less bulky methylenedioxy protecting groups are effective in obtaining hydroxy groups at the edge of GNRs through deprotection during surface-assisted reactions, while hydroxy-functionalized precursors failed to yield GNRs, indicating that the protection/deprotection method also works in on-surface synthesis (Fig. 1a). The first-principles studies investigated the mechanism, which revealed some findings including the effect of methylenedioxy functionalization on the dehydrogenation path and the deprotection mechanism of methylenedioxy groups. This result unveils one of the essential design policies for edge-functionalization of bottom-up GNRs, which is one of the critical elements for future GNR electronics.

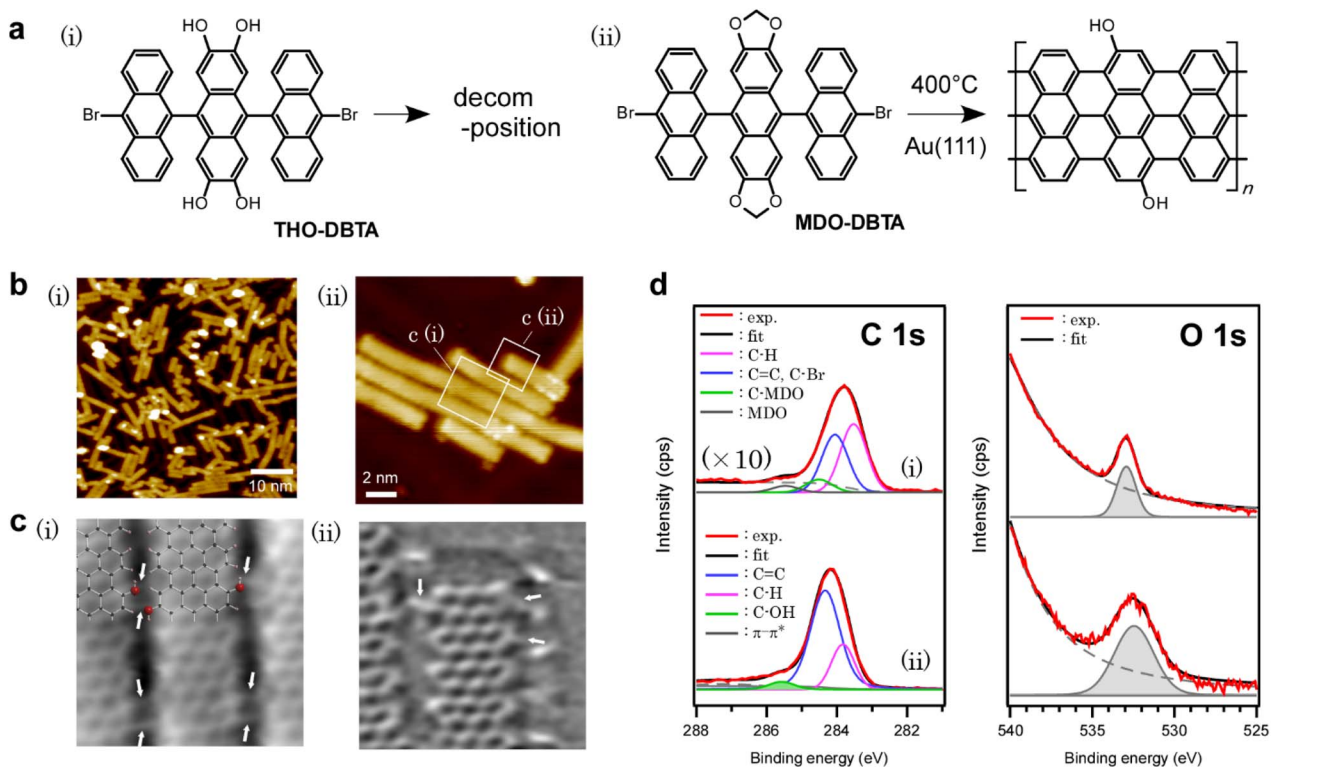

Fig. 1 (a) The chemical formulae of precursor molecules used in this study. One of the representative structures of GNRs functionalized by using hydroxy groups is shown in (ii). (b) The STM image of GNRs fabricated using an MDO-DBTA precursor. The wide scan image (i) and the magnified STM image (ii) of the obtained GNR. (c) (i) The nc-AFM image of GNRs with CO functionalized tips. The white arrows indicate the hydroxy groups. (ii) Another nc-AFM image (Laplacian filtered to clarify the ribbon edges) indicating the transition of the hydroxy groups (max: −2.3 Hz and min: −7.2 Hz for (i); max: −1.8 Hz and min: −6.1 Hz for (ii)). (d) The experimental spectra of C 1s and O 1s X-ray photoemission lines. (i) MDO-DBTA precursor as-deposited on Au(111), and (ii) the obtained GNRs with high coverage on Au(111). The backgrounds are shown with broken gray lines.

© 2022 The Author(s). Published by the Royal Society of Chemistry

Experimental

Syntheses of precursors

The synthesis procedure, NMR (Fig. S1–S10†) and mass spectrometry (Fig. S11–S22†) spectra of precursors, and X-ray single crystal structure of MDO-DBTA (Fig. S23†) are summarized in the ESI.†

Surface-assisted syntheses

Surface-assisted syntheses were carried out under ultra-high vacuum (UHV) at a base pressure of 2×10^{-8} Pa. The surfaces of Au(111)/mica substrates (Phasis, Switzerland) were cleaned by repeated cycles of 0.7 kV Ar^+ sputtering and annealing at 450 °C. Precursor molecules were sublimated from a Ta crucible held at ~350 °C onto the Au(111) surface held at 200 °C, with a typical deposition rate of ~1 Å min^{-1}. After deposition, the samples were post-annealed *in situ*. The typical post-annealing temperature was ~400 °C.

STM and non-contact AFM characterization

Scanning tunneling microscope (STM) characterization shown in Fig. 1b(i) was carried out at UNISOKU USM1400S-4P with a base pressure of 7×10^{-9} Pa at 77.6 K, with the topographic images recorded in constant-current mode using PtIr tips at I_t/V_s = 20 pA/−1.5 V. For STS measurements, all dI/dV signals were recorded using a lock-in amplifier with a sinusoidal voltage of 30 mV (r.m.s). The dI/dV spectra were acquired under open-feedback conditions. The STM data were processed using the SPIP software.

The STM [Fig. 1b(ii)] and non-contact atomic force microscopy (nc-AFM) experiments (Fig. 1c) were conducted using an Omicron low-temperature STM/AFM system at a base pressure of 4×10^{-9} Pa at 4.8 K. Single-crystalline Au(111) was cleaned by repeated cycles of 2 keV Ar^+ sputtering and annealing at 500 °C. The GNR/Au(111) sample was exposed to CO gas at 6 K. A CO molecule on the surface was picked up to attach to the tip apex to obtain high-resolution AFM images.[35] A tuning fork with an etched W tip was used as a force sensor (resonance frequency of 21.2 kHz and quality factor of 4×10^4). For the AFM images, the frequency shift was measured in constant height mode at V_s = 0 mV and an oscillation amplitude of 0.1 nm with a CO-terminal tip. The tip height for the AFM images was 70 pm closer to the surface than the set-point height determined by STM over the bare Au surface. The STM image shown in Fig. 1b(ii) was obtained in constant current mode at V_s = 30 mV and I_t = 20 pA.

XPS characterization

X-ray photoemission spectroscopy (XPS) experiments (Kratos AXIS-HSi) were performed at 2×10^{-7} Pa at room temperature using monochromatized Al Kα line ($h\nu$ = 1486.6 eV) radiation. The sample was transferred in air from the STM chamber to the XPS chamber for XPS measurement. Energy calibration was performed using the Au Fermi edge in each sample, and the energy resolution was set to 550 meV for all spectra. The background subtraction was performed using the Shirley method. In the background subtraction of O 1s XPS spectra presented in Fig. 1d, an Au $4p_{3/2}$ peak centered at 546 eV (not shown) was also subtracted. All spectra were normalized relative to the total emission in the wide scan spectra.

Computational details

All computational calculations were performed using the DFT code OpenMX.[36] The exchange–correlation potential was treated within the generalized gradient approximation using the Perdew–Burke–Ernzerhof functional.[37] Electron–ion interactions were described by norm-conserving pseudopotentials with partial core correction.[38,39] Pseudoatomic orbitals centered on atomic sites were used as the basis function set,[40] with the corresponding basis functions specified by Au7.0-s2p2d2f1, C6.0-s2p2d1, H5.0-s2p1, and O7.0-s2p2d1. The van der Waals corrections were included by using a semiempirical DFT-D2 method.[41] The unit cell includes a repeated slab of the $(9 \times 4\sqrt{3})$ Au(111) surface with a a >1 nm thick vacuum layer. The effective screening medium (ESM) method was used for handling the repeated slab model with periodic repetition in the lateral directions.[42,43] Geometry optimizations were performed under a three-dimensional periodic boundary condition. The slab contains three layers of Au, and the atoms in the bottom layer of Au slabs were fixed and the others were relaxed. The minimum energy path was determined using the nudged elastic band (NEB) method.[44] Convergence criteria for forces acting on atoms were set to 0.01 and 0.15 eV $Å^{-1}$ for geometry optimization and NEB calculations, respectively.

The absolute binding energies of oxygen 1s photoemission lines in precursors and GNRs on Au(111) are estimated in the framework of DFT.[45] The absolute binding energy E_b^{bulk} for an arbitrary gapped system can be estimated using the equation in the literature[45] as follows:

$$E_b^{bulk} = E_f^{(0)}(N-1) - E_i^{(0)}(N) + \mu_0 \quad (1)$$

where $E_i^{(0)}(N)$, $E_f^{(0)}(N-1)$ and μ_0 are the intrinsic total energy of the ground state of N electrons, the intrinsic total energy of the excited state of $N-1$ electrons with a core hole, and the chemical potential, respectively. We assumed that the chemical potential μ for the initial and final states are identical due to a very large N. For metals, on the other hand, eqn (1) is further reorganized and yields the following formula:[45]

$$E_b^{metal} = E_f^{(0)}(N) - E_i^{(0)}(N) \quad (2)$$

In this study, the binding energy of O 1s photoemission lines in precursors was estimated using eqn (1), while that in GNRs on Au was better described by using eqn (2), possibly due to mid-gap state formation in the latter case.

Results and discussion

The precursor molecules used in this study are methylenedioxy-dibromotrianthracene (MDO-DBTA) and tetrahydroxy-dibromotrianthracene (THO-DBTA). The structural formulae of the precursors are shown in Fig. 1a.

© 2022 The Author(s). Published by the Royal Society of Chemistry

Table 1 The calculated and experimental XPS binding energies of O 1s photoemission lines

	Calculated binding energy	Experimental binding energy
MDO-DBTA precursor on Au(111)	533.1 eV	532.9 eV
HO-N7AGNR on Au(111)	532.2 eV	532.4 eV
MDO-N7AGNR on Au(111)	532.0 eV	—
Quinone-N7AGNR on Au(111)	527.6 eV	

After depositing the precursor onto Au(111) at 200 °C in an ultra-high vacuum, the sample was annealed at 400 °C for cyclo-dehydrogenation. The STM image is shown in Fig. 1b, in which the fully planarized GNRs with an apparent height of ∼1.8 Å from MDO-DBTA were observed. Of the precursors tested (MDO-DBTA and THO-DBTA), only MDO-DBTA was able to obtain GNRs successfully. The possible reason why THO-DBTA failed to yield GNRs is ascribed to the decomposition of THO-DBTA molecules under ambient conditions (see Fig. S24† in the ESI for details). The XPS spectra shown in Fig. 1d indicate that the formed GNRs contain functional groups with oxygen. The experimental O1s spectrum of GNRs shown in Fig. 1d(ii) was fitted by a peak at 532.4 eV. The integrated intensity ratio of the O 1s and C 1s photoemissions obtained with GNRs are compared to those obtained with MDO-DBTA precursors as-deposited on Au(111). The peak intensity ratio analysis suggests that ∼20% of the oxygen on precursor edges remained on GNRs [Fig. 1d(ii)]. The peaks in the XPS spectra were assigned using the estimated photoemission lines in the framework of the DFT[45] (the models we used are depicted in Fig. S25† in the ESI). The estimated absolute binding energies $E_b^{calc.}$ for precursors and GNRs adsorbed on Au(111) are summarized in Table 1. The $E_b^{calc.}$ of O 1s photoemission lines of MDO-DBTA on Au(111) was estimated to be 533.1 eV, which is directly comparable to the experimental value (532.9 eV). This result supports the validity of our calculation method. The $E_b^{calc.}$ of O 1s photoemission lines of GNRs on Au(111) was calculated accordingly and summarized in Table 1. The O 1s $E_b^{calc.}$ of GNRs with edges functionalized by methylenedioxy functional groups is estimated to be 532.0 eV (see Fig. S25† for the model), which is almost identical to that estimated for hydroxy groups (532.2 eV). The O 1s $E_b^{calc.}$ of GNRs with edges functionalized by quinones, on the other hand, is estimated to be 527.6 eV, which clearly deviates from our experimental value with GNRs (532.2 eV). This result indicates that the obtained GNR has either hydroxy or methylenedioxy groups on the edges. Further analysis is required to determine the edge structure.

The chemical structure of the obtained GNR was further confirmed in detail using nc-AFM images with a tip functionalized by a CO molecule (Fig. 1c).[35] Beside a GNR framework, functional groups other than hydrogen were observed on GNR edges [indicated by white arrows in Fig. 1c(i) and (ii)], which we attributed to the hydroxy groups referring to the XPS results (Fig. 1d and Table 1) and simulated nc-AFM images (Fig. S26† in the ESI). In the area with closely packed aligned GNRs shown in Fig. 1b(ii), we considered two types of atomistic models, one hydroxy or two hydroxy groups at each GNR edge (see Fig. S27† for the model and results), and concluded that the inter-GNR distance observed in Fig. 1b(ii) is too small for assuming two hydroxy groups at each GNR edge. The lateral inter-GNR O···H interactions with a projected length of ∼2.4 Å were estimated from the scaled atomistic models of the nc-AFM images, which is comparable to 2.49 Å in a closely packed and aligned GNR model with one hydroxy group at each GNR edge. It is also noteworthy that some functional groups appeared to hop to the adjacent anthracene, which was not previously functionalized by methylenedioxy [Fig. 1c(ii)]. We assume that detached formaldehyde, formed by the cleavage of methylenedioxy, binds to the active site during the cyclo-dehydrogenation process. The effect of the random distribution of hydroxy groups is discussed in the ESI (Fig. S28†), showing that the distribution does not largely affect the density of states (DOS) of GNRs when the amount is the same.

In order to clarify the effect of methylenedioxy functionalization and give an explanation to the experimental results presented above, the cyclo-dehydrogenation process was investigated using DFT and NEB methods based on previous studies.[27,46,47] The model we used is a polymer containing six anthracene units adsorbed on Au(111) with a periodic boundary condition. The minimum energy path for the cyclo-dehydrogenation process is summarized in Fig. 2 and 3. The relative total free energy (U_{tot}^{rel}) is evaluated with respect to the total energy of polymers as-deposited, named I0 (Fig. 2). One of the rate-limiting processes is the first C–C bond formation (I0 to I1) with one hydrogen atom pointing to the Au(111) surface while another hydrogen is pointing away from the surface. The activation energy (E_a; see Section 11 in the ESI† for the definition) required for the first C–C bonding formation was ∼1.5 eV in the methylenedioxy-functionalized anthracene polymer, which is larger than that estimated in the hydrogen-terminated anthracene polymer (1.35 eV).[46] This is mainly due to the larger activation energy required for biradical formation in the extended π orbital of methylenedioxy-functionalized anthracene. While π electron donation of the methylenedioxy group lowers the total free energy of I0, a larger E_a is required for biradical formation and C–C bonding formation in I1. There are a couple of possible dehydrogenation paths for anthracene polymers on Au(111), including the one suggested recently.[47] The paths of the [1,2] H shift (suggested by Blankenburg *et al.*[46] and named by Ma *et al.*[47]) and [1,3] H shift (considered by Ma *et al.*[47]) include the desorption of a hydrogen atom to Au(111), leading to the intermediate named I2 (Fig. 2 and 3). Two possible hopping paths of hydrogen pointing away from the substrate are then considered: I2 to I3 (corresponding to the [1,2] H shift) and I2 to

© 2022 The Author(s). Published by the Royal Society of Chemistry

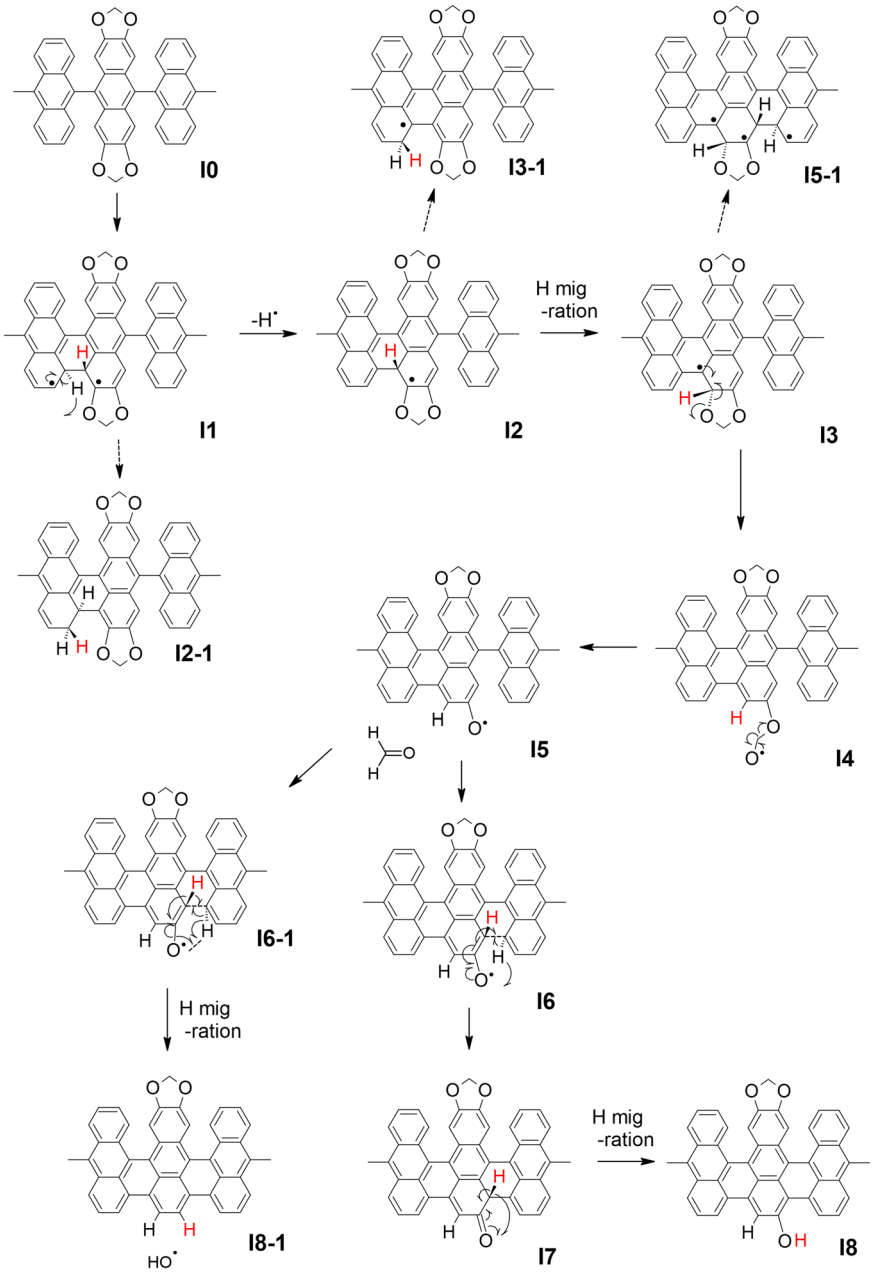

Fig. 2 The summary of the cyclo-dehydrogenation process of anthracene polymers with methylenedioxy edges.

I3-1 ([1,3] H shift). Another path (I1 to I2-1) is similar to the [1,9] shift suggested by Ma *et al.*,[47] which does not include hydrogen desorption until the formation of I2-1. As shown in Fig. 3, I2 is the intermediate preferred when the process is kinetic, while the relative total energy with respect to I0 (U_{tot}^{rel}) of I2-1 is 0.076 eV, which is lower than that of I2. It should be noted that even when the thermodynamic process chose the [1,9] shift path *via* I2-1, the methylenedioxy groups are readily cleaved during edge hydrogenation which leads to hydroxy-terminated edges (see Scheme S4† in the ESI). The E_a required from I2 to I3 was ~0.3 eV, which is smaller than that evaluated for [1,2] H-migration in anthracene polymers derived from 10,10′-dibromo-9,9′-bianthracene (DBBA) previously (~0.99 eV).[46] The smaller E_a of [1,2] H-migration in methylenedioxy-functionalized anthracene polymer is ascribed to the stabilization of radicals by the resonance effect of methylenedioxy. The U_{tot}^{rel} of I3-1 is lower than that of I3 (ΔU = 0.49 eV), which is explained by the electron donation effect of methylenedioxy using the anthracene trimer model (see Fig. S29 along with Scheme S1 and Table S1† in the ESI for the details). The E_a required from I2 to I3 was ~0.31 eV, while that of I2 to I3-1 was ~0.82 eV. The I3-1 step will lead to GNRs with methylenedioxy groups remaining intact on the edges, which are not the main product in our experiment. This result indicates that I3 was chosen as a consequence of the kinetic hydrogen hopping process.

The subsequent process after I3 is investigated using anthracene polymer models on Au(111) as follows (Fig. 2 and 3). It should be noted that the following process is one of the

© 2022 The Author(s). Published by the Royal Society of Chemistry

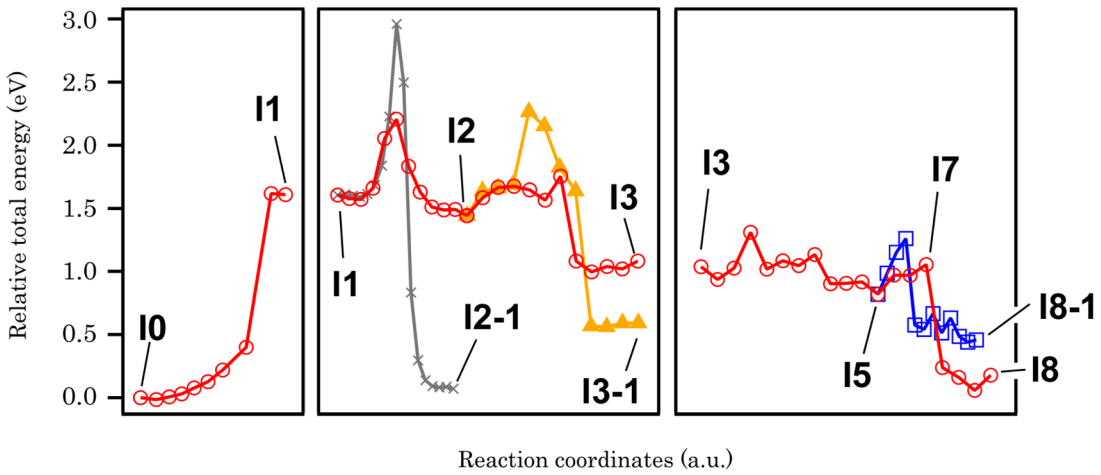

Fig. 3 The minimum energy paths of cyclo-dehydrogenation and deprotection of a methylenedioxy-functionalized anthracene polymer derived from NEB analysis.

possible dehydrogenation paths, while other paths are also suggested in the ESI (Scheme S2–S4†). After I3, we found that methylenedioxy cleavage occurs before another C–C bond formation (I4). While the $U_{\mathrm{tot}}^{\mathrm{rel}}$ of I5-1 (see Fig. 2 for the structure) is 2.49 eV, that of I5 is 0.82 eV, which is a path with lower energy for cyclo-dehydrogenation. The methylenedioxy group is cleaved and yields formaldehyde, leaving an oxygen radical on the edge, as depicted in I5. As previously stated in I1, one hydrogen atom is pointed to the surface while the other one is pointed away from the surface. There are two possible paths for the dehydrogenation of two hydrogen atoms in I5: I5 to I8 and I5 to I8-1 (Fig. 2). From I5 to I8-1, the hydrogen atom hops to the bottom of the hydroxy group, which detaches the hydroxyl ion and yields hydrogen-terminated GNRs (I8-1). From I5 to I8, the hydrogen atom pointed to the surface is detached before hydrogen hopping (I7). The hydrogen pointed away from the surface will hop and terminate hydroxyl groups, yielding GNRs with hydroxy termination (I8). The energetics of the process mentioned above are summarized in Fig. 3, which reveals that GNRs with hydroxy termination (I8) are the most kinetically preferable product. The E_{a} required for hydrogen-terminated GNRs (I8-1), though, is comparable to or smaller than the E_{a} required in the other processes. The E_{a} from I5 to I8-1 is 0.48 eV, which is larger than that required from I5 to I8 (0.23 eV) but not large enough to prevent hydrogen hopping from I5 to I8-1. This is probably why we obtained a mixture of hydroxy-terminated and hydrogen-terminated edges.

Finally, let us refer to the electronic structure of GNRs with hydroxy edges. The band gap of GNRs is somewhat controversial from experimental and theoretical viewpoints. The band gap of a free-standing GNR with seven carbon dimers in width (7AGNR), for example, was estimated to be 1.57 eV from our DFT calculation at the GGA-PBE level (Fig. S30†), while GW approximation estimated >3.7 eV for 7AGNR.[48] Although it is known that DFT can underestimate band gaps, the extraordinarily large band gap estimated in GW approximation remains elusive. The experimental determination of the 7AGNR band gap was also challenging.[49] Fourier-transform scanning tunneling spectroscopy (FT-STS) was employed to investigate the band dispersion and identify the valence band of 7AGNR,[50] in which a series of STS spectra were corrected along the GNR long axis and Fourier-transformed. A careful angle-resolved photoemission spectroscopy (ARPES) measurement revealed another hidden HOMO band with an energy separation of only ~60 meV to the second sub-band.[51] The HOMO level pinning was also reported for various bottom-up GNRs on metal substrates,[52] which is caused by charge transfer from GNRs to substrates. For the band gap of GNRs with hydroxy edges developed in this study, the band gap of the free-standing hydroxy-terminated GNR was determined to be $E_{\mathrm{g,\ DFT}} = 1.41$ eV using DFT at the GGA-PBE level, which is smaller than that of 7AGNR ($E_{\mathrm{g,\ DFT}} = 1.57$ eV) with hydrogen-terminated edges (see Fig. S30† for the model structure and the band dispersion), partially because of additional orbital nodes in the HOMO of the GNR with hydroxy groups (Fig. S31†). Although the non-uniformity of the structure makes the complementary experimental evaluation of the band gap using FT-STS or ARPES difficult, the STS spectra revealed that some part of GNRs have an electronic structure distinct from that of 7AGNR. Fig. 4a summarizes a series of STS spectra recorded on GNR/Au(111) and Au(111). Unlike 7AGNR, in which the valence band onset was observed at ~−0.87 eV,[51] the valence band features are observed at ~−0.60 eV. On the other hand, the LUMO onset required a close tip-sample separation to identify (set-point 0.5 nA). The LUMO onset was observed at 1.64 eV as a peak [Fig. 4a(v) and (vi)] or a kink beside the LUMO+1 peak [Fig. 4a(vii)], which is similar to the spectrum of 7AGNR. These phenomena are qualitatively reproduced by DFT at the GGA-PBE level, as shown in Fig. 4b. As the onset of the HOMO band is shifted to the Fermi level while the LUMO band position is unaffected, the band gap of GNRs is lowered after hydroxy functionalization. The electron density difference upon GNR adsorption on Au(111) (Fig. 4c) indicates a larger amount of charge transfer from the hydroxy-terminated GNR to the Au

© 2022 The Author(s). Published by the Royal Society of Chemistry

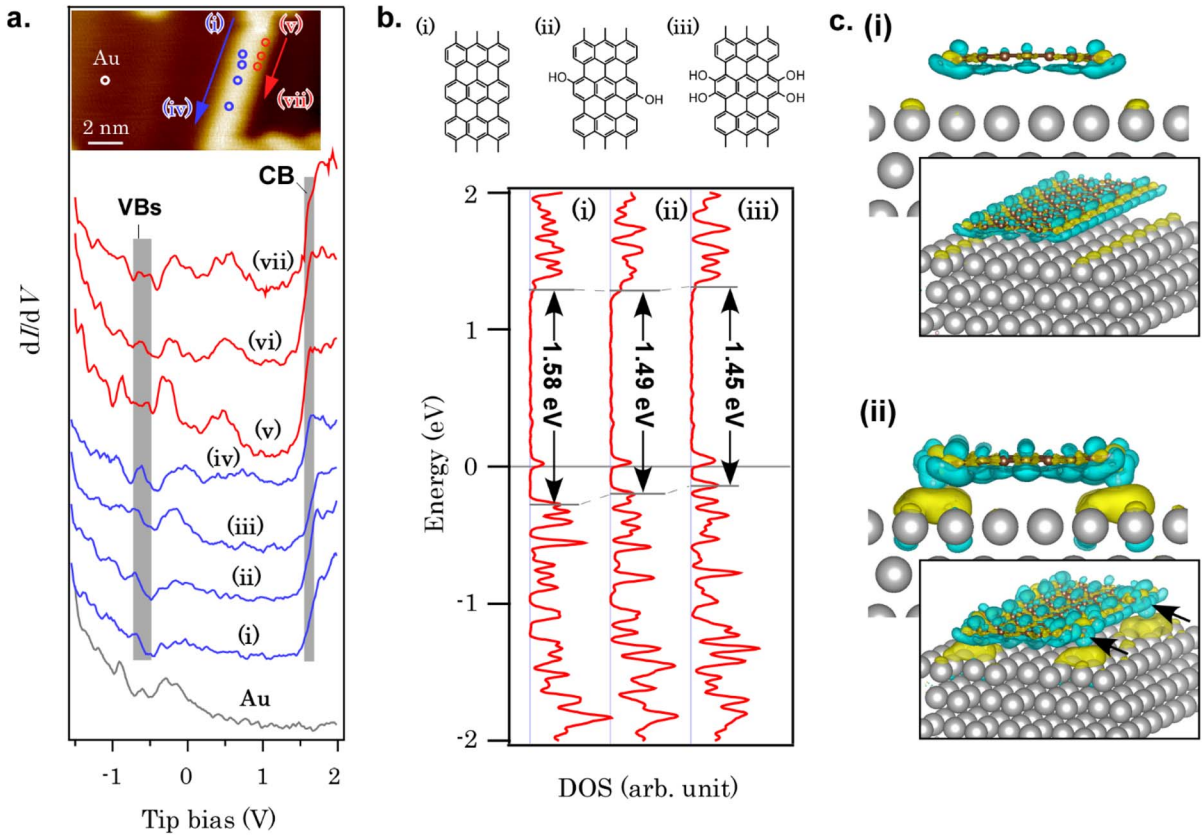

Fig. 4 (a) A series of STS spectra taken on GNRs and the pristine Au(111) surface at 77.5 K. The set-point for the spectra is 0.2 nA [(i–iv)] and 0.5 nA [Au and (v–vii)]. The STM image shown in the inset was obtained at 0.9 nA/−0.6 V. (b) The projected density of states (PDOS) of GNRs adsorbed on Au(111). The considered models are (i) 7AGNR and (ii) GNRs functionalized by two hydroxy groups, and (iii) four hydroxy groups per three anthracene units, respectively. All models contain Au slabs with periodic boundary conditions. (c) The electron density difference induced by the adsorption of GNRs on Au(111). The considered models are (i) 7AGNR and (ii) GNRs with four hydroxy groups per unit cell, respectively. The isosurface is depicted at 4.88×10^{-4} e bohr^{-3}. The blue and yellow isosurface represents depletion and accumulation of electrons, respectively.

substrate when compared with 7AGNR/Au(111). The electron densities on the hydroxy groups are significantly depleted, giving rise to a large number of transferred electrons below the hydroxy groups. The large interface dipole is probably responsible for the deviation from Fermi-level pinning tendencies in hydrogen-terminated GNRs.[52] Although further studies such as ARPES using a more uniform sample are required for the precise assignments of GNR valence bands, this result implies that edge functionalization can modify the GNR-electrode interface band alignment, which could be useful for overcoming the carrier-injection barrier in the GNR devices.[17]

Conclusions

We demonstrated the bottom-up growth of GNRs with edges functionalized by hydroxy groups. The protection of hydroxy groups on precursor molecules using methylenedioxy yielded GNR edges with partial hydroxy functionalization, while precursors with hydroxy groups did not yield GNRs due to precursor decomposition. The first-principles study on the kinetics of the cyclo-dehydrogenation process revealed that the migration of the dehydrogenated hydrogen to the bottom of methylenedioxy is kinetically chosen, leading to the on-surface deprotection of the methylenedioxy groups. The STS results combined with the first-principles DFT calculations revealed a large interface dipole derived from charge transfer from hydroxy groups to the substrate, which makes the HOMO band closer to the Fermi level while the LUMO onset position is not primarily affected. Uncontrollable hydroxy modification with the present technique could be a disadvantage if further modification of hydroxy groups (such as quinoid formation) is intended. However, this randomness is not an issue if we focus solely on the electronic structure modification with hydroxy groups, which was shown by our DFT studies. This is because weak electron donations from hydroxy groups do not largely contribute to the π resonance. This result not only gives us some fruitful insights into on-surface chemistry but also gives us a new strategy to obtain GNRs with various edge terminations through deprotection of protected edge groups, which is helpful for high-performance devices with small junction capacitance.

Conflicts of interest

There are no conflicts to declare.

© 2022 The Author(s). Published by the Royal Society of Chemistry

Author contributions

M. Ohtomo, H. H., H. Y., and S. S. conceived the experiments. H. H., M. K., R. H., N. A., and H. Y. synthesized the molecules. N. A. performed an X-ray single crystal analysis. M. Ohtomo and J. Y. designed, carried out, and analyzed the STM and XPS experiments under the supervision of S. S. M. Ohtomo and H. J. carried out the DFT study, including the XPS simulation under the supervision of M. Ohfuchi and S. S. A. S. designed, carried out and analyzed the nc-AFM experiments and simulations under the supervision of Y. S. M. Ohtomo, H. H. and A. S. wrote the manuscript. All authors discussed the results and commented on the manuscript at all stages.

Acknowledgements

This work was supported by JST CREST (no. JPMJCR15F1), JST PRESTO (no. JPMJPR21AC), JSPS KAKENHI (grant nos JP20H02711, JP20H02816, JP20H05833, JP18H01807, JP20H05178, JP20H05849, and JP20H00379), from the Ministry of Education, Culture, Sports, Science and Technology (MEXT), Japan. This work was also supported by the Toshiaki Ogasawara Memorial Foundation. We thank Prof. T. Ozaki (Univ. of Tokyo) for fruitful discussion and technical support. This study was partly supported by the NIMS Molecule & Material Synthesis Platform in the "Nanotechnology Platform Project" operated by MEXT, Japan.

References

1 M. Romagnoli, V. Sorianello, M. Midrio, F. H. L. Koppens, C. Huyghebaert, D. Neumaier, P. Galli, W. Templ, A. D'Errico and A. C. Ferrari, *Nat. Rev. Mater.*, 2018, **3**, 392–414.

2 A. Brenneis, F. Schade, S. Drieschner, F. Heimbach, H. Karl, J. A. Garrido and A. W. Holleitner, *Sci. Rep.*, 2016, **6**, 35654.

3 M. Ono, M. Hata, M. Tsunekawa, K. Nozaki, H. Sumikura, H. Chiba and M. Notomi, *Nat. Photonics*, 2020, **14**, 37–43.

4 S. Hirose, M. Norimatsu, K. Suzuki, Y. Yagishita, Y. Suwa, T. Kurosawa, K. Kawamura, Y. Mizuno, D. Kondo and T. Iwai, *Extended Abstracts of the 2015 International Conference on Solid State Devices and Materials (SSDM)*, 2015, pp. 454–455.

5 Q. Cao, J. Tersoff, D. B. Farmer, Y. Zhu and S.-J. Han, *Science*, 2017, **356**, 1369–1372.

6 G. Hills, C. Lau, A. Wright, S. Fuller, M. D. Bishop, T. Srimani, P. Kanhaiya, R. Ho, A. Amer, Y. Stein, D. Murphy, Arvind, A. Chandrakasan and M. M. Shulaker, *Nature*, 2019, **572**, 595–602.

7 J. Cai, P. Ruffieux, R. Jaafar, M. Bieri, T. Braun, S. Blankenburg, M. Muoth, A. P. Seitsonen, M. Saleh, X. Feng, K. Müllen and R. Fasel, *Nature*, 2010, **466**, 470.

8 L. Talirz, H. Söde, T. Dumslaff, S. Wang, J. R. Sanchez-Valencia, J. Liu, P. Shinde, C. A. Pignedoli, L. Liang, V. Meunier, N. C. Plumb, M. Shi, X. Feng, A. Narita, K. Müllen, R. Fasel and P. Ruffieux, *ACS Nano*, 2017, **11**, 1380–1388.

9 A. Kimouche, M. M. Ervasti, R. Drost, S. Halonen, A. Harju, P. M. Joensuu, J. Sainio and P. Liljeroth, *Nat. Commun.*, 2015, **6**, 10177.

10 J. Yamaguchi, H. Hayashi, H. Jippo, A. Shiotari, M. Ohtomo, M. Sakakura, N. Hieda, N. Aratani, M. Ohfuchi, Y. Sugimoto, H. Yamada and S. Sato, *Commun. Mater.*, 2020, **1**, 36.

11 P. Ruffieux, S. Wang, B. Yang, C. Sánchez-Sánchez, J. Liu, T. Dienel, L. Talirz, P. Shinde, C. A. Pignedoli, D. Passerone, T. Dumslaff, X. Feng, K. Müllen and R. Fasel, *Nature*, 2016, **531**, 489–492.

12 X.-Y. Wang, J. I. Urgel, G. B. Barin, K. Eimre, M. Di Giovannantonio, A. Milani, M. Tommasini, C. A. Pignedoli, P. Ruffieux, X. Feng, R. Fasel, K. Müllen and A. Narita, *J. Am. Chem. Soc.*, 2018, **140**, 9104–9107.

13 O. Gröning, S. Wang, X. Yao, C. A. Pignedoli, G. Borin Barin, C. Daniels, A. Cupo, V. Meunier, X. Feng, A. Narita, K. Müllen, P. Ruffieux and R. Fasel, *Nature*, 2018, **560**, 209–213.

14 D. J. Rizzo, G. Veber, T. Cao, C. Bronner, T. Chen, F. Zhao, H. Rodriguez, S. G. Louie, M. F. Crommie and F. R. Fischer, *Nature*, 2018, **560**, 204–208.

15 Y. Yoon, Y. Ouyang and J. Guo, *65th Annual Device Research Conference*, 2007, pp. 271–272.

16 N. Harada, H. Jippo and S. Sato, *Appl. Phys. Express*, 2017, **10**, 074001.

17 J. P. Llinas, A. Fairbrother, G. Borin Barin, W. Shi, K. Lee, S. Wu, B. Yong Choi, R. Braganza, J. Lear, N. Kau, W. Choi, C. Chen, Z. Pedramrazi, T. Dumslaff, A. Narita, X. Feng, K. Müllen, F. Fischer, A. Zettl, P. Ruffieux, E. Yablonovitch, M. Crommie, R. Fasel and J. Bokor, *Nat. Commun.*, 2017, **8**, 633.

18 P. B. Bennett, Z. Pedramrazi, A. Madani, Y.-C. Chen, D. G. de Oteyza, C. Chen, F. R. Fischer, M. F. Crommie and J. Bokor, *Appl. Phys. Lett.*, 2013, **103**, 253114.

19 M. Ohtomo, Y. Sekine, H. Hibino and H. Yamamoto, *Appl. Phys. Lett.*, 2018, **112**, 021602.

20 M. Ohtomo, H. Jippo, H. Hayashi, J. Yamaguchi, M. Ohfuchi, H. Yamada and S. Sato, *ACS Appl. Mater. Interfaces*, 2018, **10**, 31623–31630.

21 L. Martini, Z. Chen, N. Mishra, G. B. Barin, P. Fantuzzi, P. Ruffieux, R. Fasel, X. Feng, A. Narita, C. Coletti, K. Müllen and A. Candini, *Carbon*, 2019, **146**, 36.

22 N. Richter, Z. Chen, A. Tries, T. Prechtl, A. Narita, K. Müllen, K. Asadi, M. Bonn and M. Kläui, *Sci. Rep.*, 2020, **10**, 1988.

23 M. Di Giovannantonio, O. Deniz, J. I. Urgel, R. Widmer, T. Dienel, S. Stolz, C. Sánchez-Sánchez, M. Muntwiler, T. Dumslaff, R. Berger, A. Narita, X. Feng, K. Müllen, P. Ruffieux and R. Fasel, *ACS Nano*, 2017, **12**, 74.

24 C. Moreno, M. Paradinas, M. Vilas-Varela, M. Panighel, G. Ceballos, D. Peña and A. Mugarza, *Chem. Commun.*, 2018, **54**, 9402–9405.

25 G. D. Nguyen, H.-Z. Tsai, A. A. Omrani, T. Marangoni, M. Wu, D. J. Rizzo, G. F. Rodgers, R. R. Cloke, R. A. Durr, Y. Sakai, F. Liou, A. S. Aikawa, J. R. Chelikowsky, S. G. Louie, F. R. Fischer and M. F. Crommie, *Nat. Nanotechnol.*, 2017, **12**, 1077.

© 2022 The Author(s). Published by the Royal Society of Chemistry

26 Y.-C. Chen, T. Cao, C. Chen, Z. Pedramrazi, D. Haberer, G. de OteyzaDimas, F. R. Fischer, S. G. Louie and M. F. Crommie, *Nat. Nanotechnol.*, 2015, **10**, 156–160.

27 H. Hayashi, J. Yamaguchi, H. Jippo, R. Hayashi, N. Aratani, M. Ohfuchi, S. Sato and H. Yamada, *ACS Nano*, 2017, **11**, 6204.

28 G. D. Nguyen, F. M. Toma, T. Cao, Z. Pedramrazi, C. Chen, D. J. Rizzo, T. Joshi, C. Bronner, Y.-C. Chen, M. Favaro, S. G. Louie, F. R. Fischer and M. F. Crommie, *J. Phys. Chem. C*, 2016, **120**, 2684–2687.

29 E. Carbonell-Sanromà, J. Hieulle, M. Vilas-Varela, P. Brandimarte, M. Iraola, A. Barragán, J. Li, M. Abadia, M. Corso, D. Sánchez-Portal, D. Peña and J. I. Pascual, *ACS Nano*, 2017, **11**, 7355–7361.

30 M. Panighel, S. Quiroga, P. Brandimarte, C. Moreno, A. Garcia-Lekue, M. Vilas-Varela, D. Rey, G. Sauthier, G. Ceballos, D. Peña and A. Mugarza, *ACS Nano*, 2020, **14**, 11120–11129.

31 M. Ohtomo, H. Hayashi, K. Hayashi, H. Jippo, J. Zhu, R. Hayashi, J. Yamaguchi, M. Ohfuchi, H. Yamada and S. Sato, *ChemPhysChem*, 2019, **20**, 3366–3372.

32 P. G. M. W. T. W. Greene, *Protective Groups in Organic Synthesis*, Wiley, New York, 3rd edn edn, 1999.

33 S. Kamisuki, S. Takahashi, Y. Mizushina, S. Hanashima, K. Kuramochi, S. Kobayashi, K. Sakaguchi, T. Nakata and F. Sugawara, *Tetrahedron*, 2004, **60**, 5695–5700.

34 M. Node, K. Nishide, K. Fuji and E. Fujita, *J. Org. Chem.*, 1980, **45**, 4275–4277.

35 L. Gross, F. Mohn, N. Moll, P. Liljeroth and G. Meyer, *Science*, 2009, **325**, 1110–1114.

36 *OpenMX*, **http://www.openmx-square.org/**, (accessed 24 December, 2021).

37 J. P. Perdew, K. Burke and M. Ernzerhof, *Phys. Rev. Lett.*, 1996, **77**, 3865–3868.

38 I. Morrison, D. M. Bylander and L. Kleinman, *Phys. Rev. B: Condens. Matter Mater. Phys.*, 1993, **47**, 6728–6731.

39 S. G. Louie, S. Froyen and M. L. Cohen, *Phys. Rev. B: Condens. Matter Mater. Phys.*, 1982, **26**, 1738–1742.

40 T. Ozaki, *Phys. Rev. B: Condens. Matter Mater. Phys.*, 2003, **67**, 155108.

41 S. Grimme, *J. Comput. Chem.*, 2006, **27**, 1787–1799.

42 M. Otani and O. Sugino, *Phys. Rev. B: Condens. Matter Mater. Phys.*, 2006, **73**, 115407.

43 T. Ohwaki, M. Otani, T. Ikeshoji and T. Ozaki, *J. Chem. Phys.*, 2012, **136**, 134101.

44 G. Henkelman and H. Jónsson, *J. Chem. Phys.*, 2000, **113**, 9978–9985.

45 T. Ozaki and C.-C. Lee, *Phys. Rev. Lett.*, 2017, **118**, 026401.

46 S. Blankenburg, J. Cai, P. Ruffieux, R. Jaafar, D. Passerone, X. Feng, K. Muellen, R. Fasel and C. A. Pignedoli, *ACS Nano*, 2012, **6**, 2020–2025.

47 C. Ma, Z. Xiao, P. V. Bonnesen, L. Liang, A. A. Puretzky, J. Huang, M. Kolmer, B. G. Sumpter, W. Lu, K. Hong, J. Bernholc and A.-P. Li, *Chem. Sci.*, 2021, **12**, 15637–15644.

48 L. Yang, C.-H. Park, Y.-W. Son, M. L. Cohen and S. G. Louie, *Phys. Rev. Lett.*, 2007, **99**, 186801.

49 P. Ruffieux, J. Cai, N. C. Plumb, L. Patthey, D. Prezzi, A. Ferretti, E. Molinari, X. Feng, K. Muellen, C. A. Pignedoli and R. Fasel, *ACS Nano*, 2012, **6**, 6930–6935.

50 H. Söde, L. Talirz, O. Gröning, C. A. Pignedoli, R. Berger, X. Feng, K. Müllen, R. Fasel and P. Ruffieux, *Phys. Rev. B: Condens. Matter Mater. Phys.*, 2015, **91**, 045429.

51 B. V. Senkovskiy, D. Y. Usachov, A. V. Fedorov, D. Haberer, N. Ehlen, F. R. Fischer and A. Grüneis, *2D Mater.*, 2018, **5**, 035007.

52 N. Merino-Díez, A. Garcia-Lekue, E. Carbonell-Sanromà, J. Li, M. Corso, L. Colazzo, F. Sedona, D. Sánchez-Portal, J. I. Pascual and D. G. de Oteyza, *ACS Nano*, 2017, 11661–11668.

© 2022 The Author(s). Published by the Royal Society of Chemistry